



Systemic and single cell level responses to 1 nm size biomaterials demonstrate distinct biological effects revealed by multi-omics atlas

Tao Zhang^{a,b,1}, Tingyun Lei^{a,b,1}, Ruojin Yan^b, Bo Zhou^b, Chunmei Fan^b, Yanyan Zhao^b, Shasha Yao^d, Haihua Pan^e, Yangwu Chen^b, Bingbing Wu^b, Yuwei Yang^b, Lijuan Hu^f, Shen Gu^g, Xiaoyi Chen^b, Fangyuan Bao^b, Yu Li^b, Hanqi Xie^b, Ruikang Tang^e, Xiao Chen^{b,c,**}, Zi Yin^{a,b,c,*}

^a Dr. Li Dak Sum & Yip Yio Chin Center for Stem Cells and Regenerative Medicine, and Department of Orthopedic Surgery of Sir Run Shaw Hospital, Zhejiang University School of Medicine, Hangzhou, 310058, PR China

^b Key Laboratory of Tissue Engineering and Regenerative Medicine of Zhejiang Province, School of Medicine, Zhejiang University, Hangzhou, 310058, PR China

^c China Orthopedic Regenerative Medicine Group CORMed, Hangzhou, 310058, PR China

^d Department of Orthopaedic Surgery of Sir Run Run Shaw Hospital, Zhejiang University School of Medicine, Hangzhou, 310058, PR China

^e Qiushi Academy for Advanced Studies, Zhejiang University, Hangzhou, 310058, PR China

^f Department of Pathology of the First Affiliated Hospital, Anhui University of Chinese Medicine, Hefei, 230031, PR China

^g School of Biomedical Sciences, The Chinese University of Hong Kong, Shatin, N.T, HKSAR, China

ARTICLE INFO

Keywords:

Nanoparticle
Nanocluster
Single-cell mass cytometry
RNA-Seq
Multi-omics

ABSTRACT

Although ultra-small nanoclusters (USNCs, < 2 nm) have immense application capabilities in biomedicine, the investigation on body-wide organ responses towards USNCs is scant. Here, applying a novel strategy of single-cell mass cytometry combined with Nano Genome Atlas of multi-tissues, we systematically evaluate the interactions between the host and calcium phosphate (CaP) USNCs at the organism level. Combining single-cell mass cytometry, and magnetic luminex assay results, we identify dynamic immune responses to CaP USNCs at the single cell resolution. The innate immune is initially activated and followed by adaptive immune activation, as evidenced by dynamic immune cells proportions. Furthermore, using Nano Genome Atlas of multi-tissues, we uncover CaP USNCs induce stronger activation of the immune responses in the cartilage and subchondral bone among the five local tissues while promote metabolic activities in the liver and kidney. Moreover, based on the immunological response profiles, histological evaluation of major organs and local tissue, and a body-wide transcriptomics, we demonstrate that CaP USNCs are not more hazardous than the Food and Drug Administration-approved CaP nanoparticles after 14 days of injection. Our findings provide valuable information on the future clinical applications of USNCs and introduce an innovative strategy to decipher the whole body response to implants.

1. Introduction

Due to their unique chemical, optical, electrical and magnetic properties, inorganic nanoparticles (NPs, 1–100 nm) have been extensively studied for their clinical application potentials [1–4]. Recently, as the new generation NPs, ultra-small nanoclusters (USNCs, < 2 nm), have attracted growing research interests [3,4]. With their distinct small size, USNCs displayed superior performance in biomedical imaging and

therapeutic applications [5–9]. Furthermore, USNCs demonstrated improved biological functions comparing to the conventional NPs. Previously, we developed a new calcium phosphate (CaP) USNC (≈1 nm) in the polymer-induced liquid-precursor (PILP). It was demonstrated that these new CaP USNCs could enter the tortuous subchannels of the collagen fibril (≈1.8–4 nm) to fully recover osteoporotic bones, which was much more advanced over the widely used hydroxyapatite nanoparticles (HANPs) [8]. However, the *in vivo* biosafety of USNCs was

Peer review under responsibility of KeAi Communications Co., Ltd.

* Corresponding author.

** Corresponding author. Dr. Li Dak Sum & Yip Yio Chin Center for Stem Cells and Regenerative Medicine, and Department of Orthopedic Surgery of The Second Affiliated Hospital, Zhejiang University School of Medicine, Hangzhou, 310058, PR China.

E-mail addresses: chenxiao-610@zju.edu.cn (X. Chen), yinzi@zju.edu.cn (Z. Yin).

¹ These authors contributed equally.

<https://doi.org/10.1016/j.bioactmat.2022.03.026>

Received 28 November 2021; Received in revised form 26 February 2022; Accepted 15 March 2022

Available online 26 March 2022

2452-199X/© 2022 The Authors. Publishing services by Elsevier B.V. on behalf of KeAi Communications Co. Ltd. This is an open access article under the CC BY-NC-ND license (<http://creativecommons.org/licenses/by-nc-nd/4.0/>).

still unsettled, hindering the clinical applications of this new generation of NPs.

NPs could enter the blood circulation and accumulate at multiple organs following local application, and the translocation effect is size-dependent, with a greater translocation for smaller NPs [10,11]. Current studies have examined the toxicity of NPs on a single organ or a few organs only [12–14], which is inadequate to unveil their potential risks for clinical applications. Furthermore, using just routine testing

methods, it is limited and insufficient to determine the subtle adverse effects of NPs, let alone the differences between one type of NPs and another [7,15]. The standards for nano-risk assessment are urgently needed, accompanied by supporting proof of routine toxicological analyses. Therefore, a new generation of evaluation approach is required to monitor the safety or toxicity of USNCs *in vivo* at the whole-organism scale.

Multi-omics analysis can facilitate our understanding of bio-nano

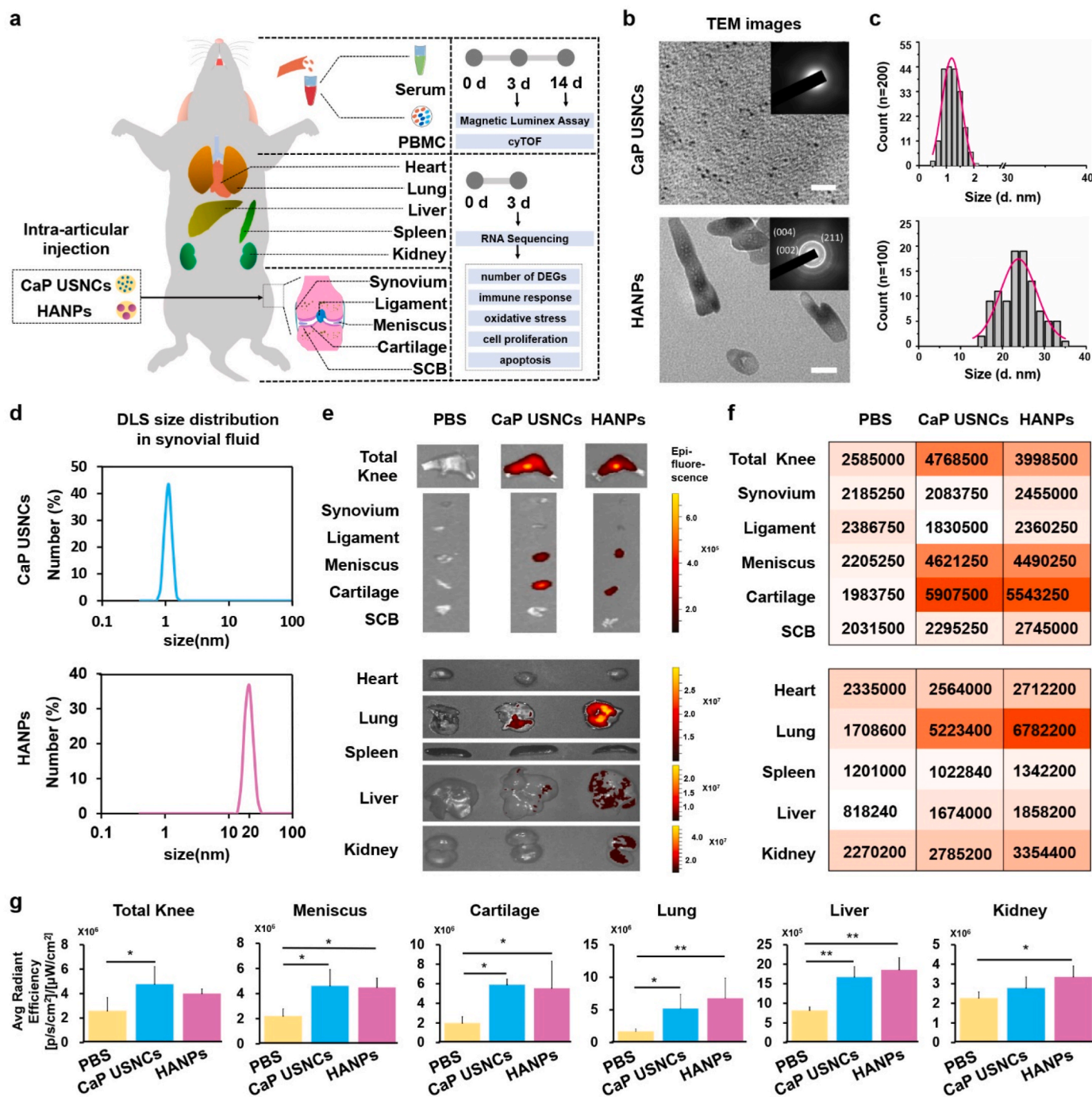


Fig. 1. Characterization and bio-distribution of the two types of CaP NPs. (a) Schematic illustration of the tissues and organs collected in this study. (b) High-resolution transmission electron microscopy (TEM) image and selected area electron diffraction (SAED) pattern (inset) of CaP USNCs, and TEM image and SAED pattern (inset) of the HANPs (bottom panel). Scale bar of the top panel, 20 nm, scale bar of the bottom panel, 50 nm. (c) The histogram of diameter distribution of the two CaP NPs. The diameter distribution of CaP USNCs is 1.21 ± 0.30 nm (N = 200), while the HANPs is 23.99 ± 4.55 nm (N = 100). (d) Stability of nanoparticles in synovial fluid. Fluorescence images (e), average radiant efficiency of signal preservation (f, g) of various organs collected from the rats 3 days after intra-articular injection. n = 5. SCB: subchondral bone. DLS: dynamic light scattering.

interactions [16]. With the development of next-generation sequencing technologies, we can concurrently characterize the transcriptome of tissues and organs in the whole body [17–19]. Furthermore, single-cell mass cytometry (CyTOF), which measures over 40 cellular parameters, can dissect phenotypic and functional alterations at the single-cell resolution [20–23]. Hence, these advanced techniques could enhance the understanding of the complex interactions between biomaterials and cells in the whole body, especially for the immune system.

In this study, combining Nano Genome Atlas (NGA) of multi-tissues [19] and CyTOF, we analyzed the systemic responses of USNCs at the organism level and evaluated the safety or toxicity differences comparing with HANPs, which are the Food and Drug Administration (FDA)-approved CaP NPs [24] (Fig. 1a). *Ex vivo* imaging of multiple tissues and organs was used to determine the biodistribution of CaP USNCs and HANPs. The distinct NP-induced foreign body reactions were determined by CyTOF, magnetic luminex assay and routine blood examination. Using RNA-seq, we decoded the acute body-wide-organ-transcriptomic responses to the two types of CaP NPs with different size. Our established multi-omics atlas view can be readily applied to other nano-risk assessments.

2. Materials and methods

2.1. Material preparation

The preparation of CaP USNCs was as described previously [8]. In brief, 4.3 g PAA (Mw = 450 kDa), 2.15 g PASP (Mw = 9–11 kDa), and 0.7248 g Na₂HPO₄ were added to 50 mL of deionized water and vigorously stirred to dissolve overnight to obtain solution A. Under vigorous stirring, 2 mL of a 0.1 M CaCl₂ solution was first added dropwise into 0.15 mL of a 0.3 g mL⁻¹ PASP solution to obtain solution B. Following, 2 mL of solution A was slowly added to solution B with vigorous stirring, and the pH value was adjusted to 7.4 with NaOH solution. Finally, we obtained CaP USNCs without any precipitation. To analyze the *in vivo* biodistribution of CaP USNCs, we labeled the calcium of CaP USNCs with calcein. Under gentle stirring, the CaP USNCs were mixed with 22.2 μL of a 10 mg mL⁻¹ calcein solution to obtain the calcein-stained CaP USNCs.

To prepare HANPs, firstly, 0.0201 g HANPs (Yuanye, China) were dissolved in 2 mL deionized water to obtain HANPs solution. Under vigorous stirring, 2 mL of the HANPs solution was added dropwise into 0.15 mL of 0.3 g mL⁻¹ PASP solution to obtain solution C. Following, 2 mL of solution A was slowly added to solution C with vigorous stirring, and the pH value was adjusted to 7.4 with NaOH solution. Finally, HANPs were obtained. To analyze the *in vivo* biodistribution of HANPs, the calcium of HANPs was labeled similarly as CaP USNCs above. HANPs were mixed with 22.2 μL of 10 mg mL⁻¹ calcein solution to obtain the calcein-stained HANPs.

To create the CON group, under vigorous stirring, 2 mL deionized water was added dropwise into 0.15 mL of 0.3 g mL⁻¹ PASP solution to obtain solution D. Subsequently, 2 mL of solution A was slowly added to solution D with vigorous stirring, and the pH value was adjusted to 7.4 with NaOH solution. Finally, a CON of 4.15 mL was obtained.

2.2. Transmission electron microscopy

TEM was performed with a Hitachi HT-7700 (Japan) operating at 120 kV. HRTEM was conducted using a JEOL JEM-2100F microscope (Japan) and operated at 200 kV. EDS spectra were collected using the JEM-2100F microscope equipped with an energy dispersive X-ray spectrometer (Oxford-T80, Nano Lab Technologies Inc., USA).

2.3. X-ray diffraction

The as-prepared samples were measured by XRD (Bruker D8 Advance, Germany) with Cu Kα radiation ($\lambda = 0.1542$ nm) operating at

an acceleration voltage of 40 kV and a current of 40 mA. The diffraction intensity data were scanned with a sampling step of 0.02° in the 2θ range from 5° to 90°.

2.4. Synovial fluid collection

Synovial fluid from pigs was collected postmortemly. Then synovial fluid was centrifuged at 1500 g for 15 min to remove the cellular component and passed through a 40 μM cell strainer to remove any large protein aggregates. The samples were stored at -20 °C until use in the described experiments.

2.5. Dynamic light scattering

The size distribution of NPs in synovial fluid was determined at 25 °C using the Zetasizer Nano S instrument (ZEN 3600, Malvern, England).

2.6. Animal exposures

Eight-week-old male SD rat or C57BL/6 mice (purchased from the SLAC Laboratory Animal, Shanghai, China) were randomly allocated to three groups. All procedures were performed with approved protocols (ZJU20210029), following the guidelines of the animal experimental center of Zhejiang University, People's Republic of China. After general anesthesia, we cut the skin between the lower pole of the patella and the tibial tubercle and bluntly separated the subcutaneous tissue to expose the patellar ligament. Under knee flexion 45°, rats were separately injected into the midpoint of the wound with 50 μL CaP USNCs, 50 μL HANPs and 50 μL CON, while 10 μL CaP USNCs, 10 μL HANPs and 10 μL CON were injected in mice at corresponding locus. The mass concentration of CaP USNCs solution was 4.31 mg mL⁻¹, while the HANPs solution was 4.19 mg mL⁻¹. The number concentration of CaP USNCs solution was 1.86 × 10¹⁸ mL⁻¹, while the HANPs solution was 6.90 × 10¹³ mL⁻¹ (Fig. S2).

2.7. Biodistribution studies

Methodology to inject the drug into the knee cavities of the rats was as depicted above. Rats were separately injected at the knee cavity with 50 μL of calcein-stained CaP USNCs, 50 μL of calcein-stained HANPs and 50 μL of 1 × PBS. 3 days after exposure, all the animals were anesthetized to perform cardiac perfusion with 1 × PBS. Organs and tissues of interests were then extracted, washed in 1 × PBS to remove excess blood and analyzed using a fluorescence imaging system (IVIS Spectrum, PerkinElmer).

2.8. Whole blood and serological sample analysis

Following the exposure, the rats were held for a post-exposure period of 3 days and 14 days. After fasting overnight, the rats were anesthetized to collect blood from inferior vena cava for whole blood and serological samples analysis. Complete blood count was conducted using a Mindray BC-5800 Automated Hematology Analyzer (Mindray Bio-Medical Electronics Equipment, Co., Ltd., Shenzhen, China) according to the manufacturer's instructions. The serum biochemical markers were assayed using an automatic biomedical analyzer (BS-240vet, Mindray, China).

2.9. Histology and TUNEL staining

At 3- and 14-day post-injection, images of the heart, lung, liver, spleen and kidney from the rats were taken and the organs were accurately weighed. The organs depicted above from other rats were immediately fixed in 4% paraformaldehyde, embedded in paraffin blocks, sectioned into 5 μm sections and mounted onto the glass slides. The knee joint was immediately fixed in 4% paraformaldehyde, decalcified with 10% EDTA for two months, and embedded in paraffin for 7

μm sections. The sections were stained with hematoxylin-eosin for microscopic analysis. TUNEL staining was performed using in situ Cell Death Detection Kit (Roche, Foster City, CA, USA) according to manufacturer's instructions.

2.10. DHE staining

Following the exposure, rats were held for a post-exposure period of 3 days. For dihydroethidium (DHE, Beyotime Institute of Biotechnology, China) staining, whole hearts were excised, washed thoroughly with ice-cold PBS and frozen in O.C.T. compound. Fresh 7 mm sections were cut with a cryostat and then incubated with the equal volume mixture using DHE (5 μM) and DAPI (1:5000, Beyotime Institute of Biotechnology, China) for 30 min at 37 °C in the dark.

2.11. RNA-seq

Three days after surgery, RNA was extracted from the heart, lung, liver, spleen, kidney, synovium, ligament, meniscus, cartilage, and subchondral bone of rats by Trizol reagent (TAKARA). Reverse transcription was conducted by SuperScript II reverse transcriptase (Invitrogen). Double strand cDNA was constructed using NEBNext mRNA second strand synthesis kit (NEB). The double strand cDNA was subsequently cleaned with AMPure XP beads (Beckman Coulter). Sequencing library was constructed by the Nextera XT kit (Illumina) and sequenced on Illumina XTen platform. RNA-seq reads data were mapped to the reference genome using TopHat and Cufflinks [25]. Expression was calculated based on counts per million (CPM). Differentially expressed genes (DEG) was calculated using DESeq2 [26] with retaining criteria of P value < 0.05. Gene ontology enrichment analysis was performed using Metascape informatics resources. Enrichment scores were calculated using the GSEA 4.0.3 software; the enrichment score of each gene ontology term was compared among different organs and tissues. The enrichment scores with positive values were those up-regulated upon CaP USNCs treatment, while the enrichment scores with negative values were those down-regulated upon CON or HANPs treatment. Heatmaps were drawn using the R package (pheatmap).

2.12. Single-cell mass cytometry

After 36 h, 3 days and 14 days of post-injection, blood was pooled from five mice in each group for each treatment to obtain sufficient cells for reliable mass cytometry. CyTOF analysis (PLT Tech Co., Ltd.) was performed as previously described [20]. Briefly, after lysis of the erythrocyte using ACK lysis buffer, the samples were washed using FACS buffer. The pooled cells were then stained with cisplatin for live dead cell distinction. Subsequently, the samples were blocked for 20 min and stained with the surface-antibodies mix for 30 min (Table S1, Table S2). After washing with the FACS buffer, the samples were fixed and stained with a DNA intercalator overnight. The cells were then washed with permeabilization buffer and stained with a mixture of intracellular antibodies (Table S1, Table S2) for 30 min. Following washes with FACS buffer and ddH₂O, the cells were analyzed using a CyTOF machine. The raw data acquired were uploaded to a Cytobank web server (Cytobank Inc.) for further data processing.

Cell populations were identified based on marker expression distribution according to standard definitions of cell type: CD4⁺ T cells (CD45⁺ CD3⁺ CD4⁺), CD8⁺ T cells (CD45⁺ CD3⁺ CD8⁺), $\gamma\delta$ T cells (CD45⁺ CD3⁺ TCR $\gamma\delta$ ⁺), B cells (CD45⁺ B220⁺), neutrophil (CD45⁺ CD11b⁺ Ly6g⁺), macrophage (CD45⁺ CD11b⁺ F4/80⁺), monocyte (CD45⁺ CD11b⁺ Ly6c⁺), DCs (CD45⁺ CD11b⁺ CD11c⁺), and NK cells (CD45⁺ NK1.1⁺).

2.13. Cytokine expression detection

A magnetic luminex assay with Mouse Premixed Multi-Analyte Kit

(R&D Systems) was used to detect serum cytokines.

2.14. Data analysis

Tissue cell heterogeneity was enumerated by xCell [27] using the RNA-seq data of the tissues. The quantitative data were presented as means \pm SD. The enrichment score of each cell population from each tissue was compared among the CON, CaP USNCs, and HANPs groups using one-way ANOVA with post hoc Tukey's test or Kruskal–Wallis test with post hoc Dunn's test in SPSS 25.0 software, with all P values less than 0.05 considered statistically significant. The significance level is presented as *P < 0.05, **P < 0.01, and ***P < 0.001.

3. Results

3.1. Characterization and bio-distribution of the two types of CaP NPs

High-resolution transmission electron microscopy (TEM) images of USNCs exhibited a uniform size of about 1 nm (Fig. 1b–d; Fig. S1c). Energy-dispersive X-ray spectroscopy (EDS) spectrum showed the presence of Ca and P elements in the CaP USNCs (Fig. S1a). Selected area electron diffraction (SAED, inset of Fig. 1b) and powder X-ray diffraction (pXRD, Fig. S1b) indicated that the USNCs were amorphous CaP. In contrast, the HANPs were loaded with rod-shaped NPs (\approx 20 nm, Fig. 1b–d; Fig. S1c). SAED (inset of Fig. 1b) and pXRD showed the (002) and (211) planes (Fig. S1b), indicating that the NPs are hydroxyapatites.

To investigate the biodistribution changes following local administration, fluorescence signals from calcein-stained CaP USNCs and calcein-stained HANPs were detected at 3-day post-injection. Comparing to the control PBS (phosphate-buffered saline) injection, the two CaP NPs resulted in strong signals of calcein in the knee joint and maximal accumulation in the meniscus and cartilage (Fig. 1e–g). In addition, CaP USNCs injection demonstrated stronger fluorescence signal of the total knee joint than HANPs injection (Fig. 1e–g). Furthermore, CaP USNCs and HANPs were found in other organs as well (Fig. 1e). Compared with PBS, there were stronger fluorescence intensities in the lung and liver for both of the CaP NPs injections (Fig. 1e–g). However, the fluorescence signals of the lung, liver and kidney from CaP USNCs were weaker than those obtained in the HANPs (Fig. 1e–g).

Next, we analyzed the body-wide responses of the both CaP NPs after intra-articular injection. First, no abnormal daily activities or symptoms were observed for all animals during the whole exposure. The two types of CaP NPs did not induce abnormal liver function (represented by the levels of markers TBIL, AKP, ALT and AST), kidney function (CREA and BUN), or the components of blood cells in rats at 3-day post-injection (Fig. S3a) and 14-day post-injection (Fig. S3b). CaP USNCs caused slight tissue hyperplasia along the knee joint at 3-day post-injection, and this effect disappeared at 14-day post-injection (Fig. S4a). Furthermore, compared with the CON group, no noticeable injury or inflammation was observed in the ligament, meniscus, or subchondral bone of CaP USNC and HANP groups at 3-day post-injection (Fig. S5) and 14-day post-injection (Fig. S6) by hematoxylin and eosin (H&E) staining. There was no obvious difference in the appearance and relative organ weight of the heart, lung, liver, spleen and kidney among the three groups after sacrificing all the rats at 3-day post-injection (Fig. S4a) and 14-day post-injection (Fig. S4a, b). Furthermore, no noticeable damage or inflammation was detected in the heart, lung, spleen, and kidney of the three groups at 3 days post-injection (Fig. S5) and 14-day post-injection (Fig. S6) by H&E staining.

3.2. Innate immune activation in blood after 3-day exposure to the two types of CaP NPs

To dissect the systemic immunological responses, single-cell mass cytometry was conducted on the peripheral blood of the animals. Using

visNE analysis, the nine immune cell populations were identified, including B cells, CD4⁺ T cells, CD8⁺ T cells, $\gamma\delta$ T cells, neutrophils, macrophages, monocytes, dendritic cells (DCs) and natural killer (NK) cells (Fig. 2a–c; Fig. 3a–c). The SPADE (spanning tree progression analysis of density-normalized events) algorithm was used to identify the nine immune subpopulations and to compare the abundance of the immune cells among the three groups (Figs. 2d and 3d; Figs. S7 and 8).

After 36-h treatments, the proportion of neutrophils was higher in

CaP USNC and HANP groups compared with CON group. Among them, HANP group showed the highest frequency (Fig. S9). Although the proportions of the macrophage were similar among three groups, HANPs induced higher frequency of M1 phenotype (Fig. S10).

After 3-day treatments, the total proportion of innate immune cells was higher in the CaP USNC and HANP groups comparing to the CON group, which indicated that the innate immune cells were activated in blood at day 3 (Fig. 2e). Specifically, both the CaP NP treatments

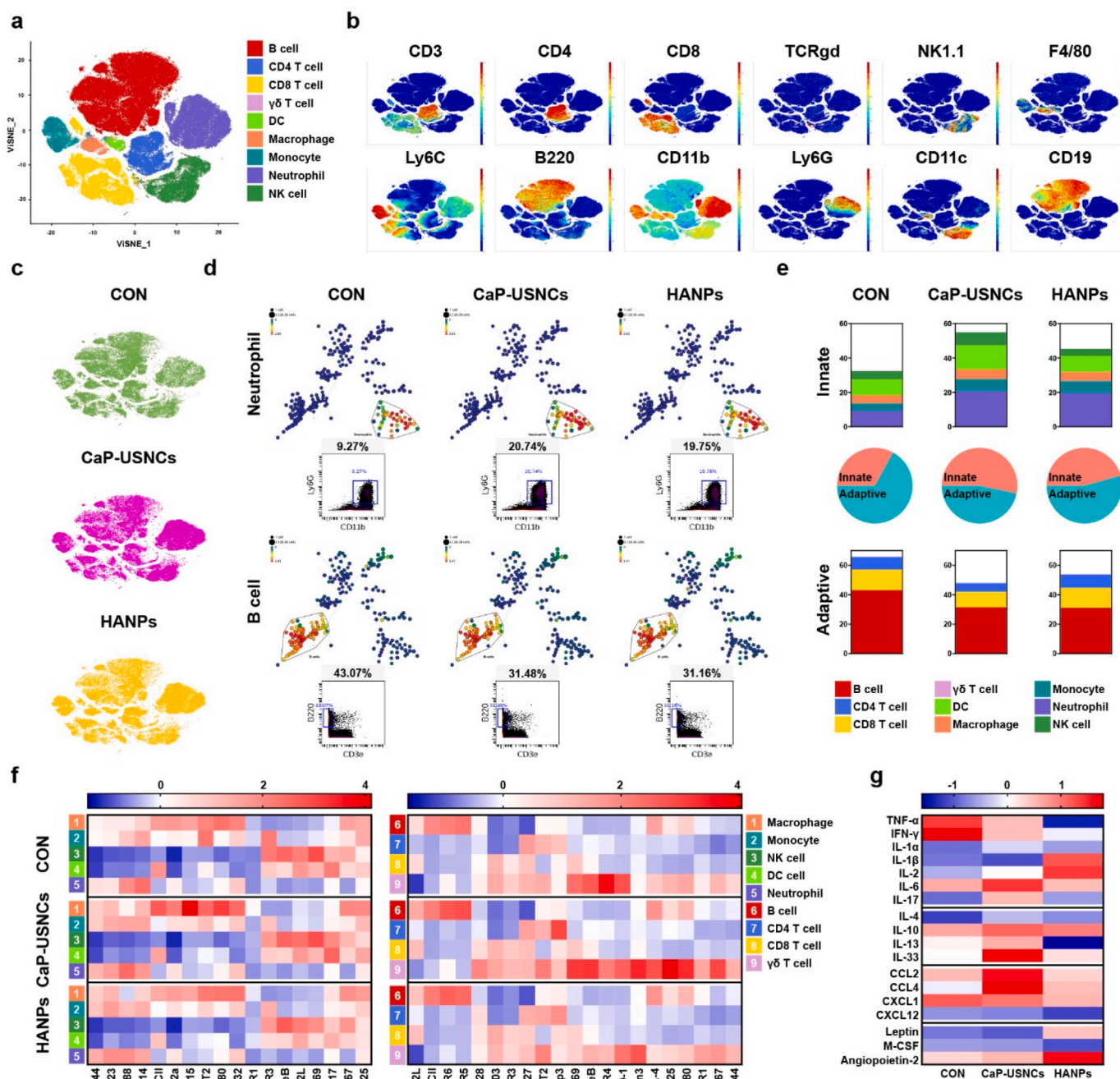


Fig. 2. The innate immune activation in blood after 3-day exposure to the two types of CaP NPs. (a) visNE algorithms identified nine major immune cell populations. (b) Markers used for major immune cell subset identification, including CD3, CD4, CD8, TCRgd, NK1.1, F4/80, Ly6C, B220, CD11b, Ly6G, CD11c, and CD19. In visNE, each dot represents a single cell, and the color gradient represents each marker's intensity. (c) Distribution of the nine immune cell populations in the three groups using the visNE algorithms. (d) The SPADE tree and dot plots analysis indicating the abundance of neutrophils and B cells in each group on day 3. In the SPADE diagram, node size represents the number of cells, and the colored gradient correlates with the expression of the marker's median intensity. (e) The frequencies of adaptive and innate immune cells as calculated from the SPADE analysis. (f) Heatmap showing the expression of functional markers in innate immune cells and adaptive immune cells among the three groups. (g) Magnetic luminex assay detection of serum cytokines in mice.

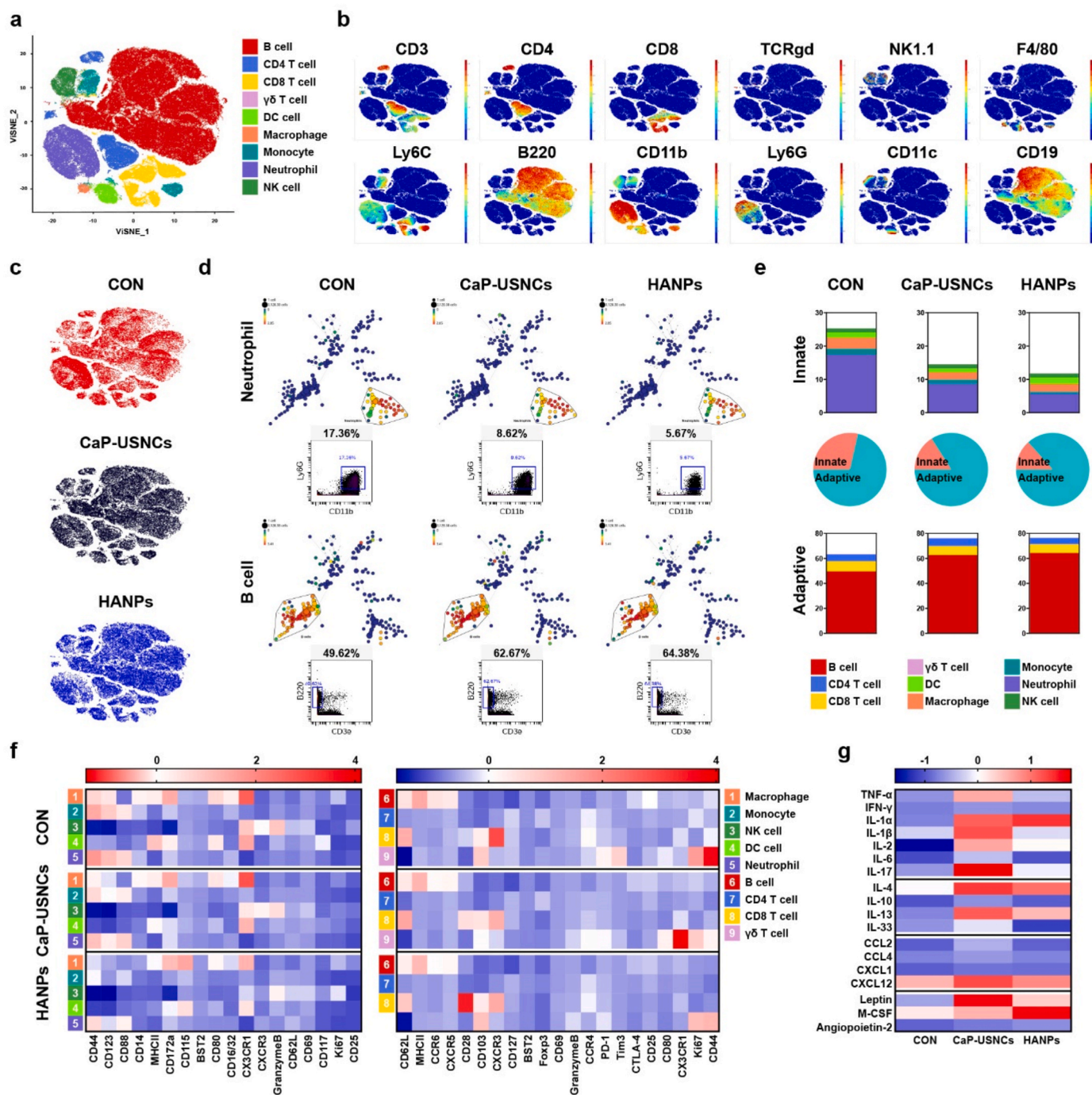


Fig. 3. The adaptive immune cells activation in blood after 14-day exposure to the two types of CaP NPs. (a) viSNE algorithms identified nine major immune cell populations. (b) Markers used for major immune cell subset identification, including CD3, CD4, CD8, TCRgd, NK1.1, F4/80, Ly6C, B220, CD11b, Ly6G, CD11c, and CD19. In viSNE, each dot represents a single cell, and the color gradient represents each marker's intensity. (c) Distribution of the nine immune cell populations in the three groups using the viSNE algorithms. (d) The SPADE tree and dot plots analysis indicating the abundance of neutrophils and B cells in each group. In the SPADE diagram, node size represents the number of cells, and the colored gradient correlates with the expression of the marker's median intensity. (e) The frequencies of adaptive and innate immune cells on day 14, as calculated from the SPADE analysis. (f) Heatmap showing the expression of functional markers in innate immune cells and adaptive immune cells among the three groups. (g) Magnetic luminex assay detection of serum cytokines in mice.

resulted in higher proportions of monocytes, macrophages, neutrophils, NK cells, and DCs (Fig. 2d and e). The proportions of DCs and NK cells were higher in the CaP USNC group than in the HANP and CON groups (Fig. 2e). The proportion of B cells was lower in both the CaP USNC and HANP groups compared with the CON group (Fig. 2d and e). The proportions of CD8⁺ T cells and CD4⁺ T cells were lower in the CaP USNC group than in the CON group (Fig. 2e). There was no obvious difference in the proportion of $\gamma\delta$ T cells among the three groups. To further explore

functional differences in the immune subpopulations, the expression patterns of functional markers in various immune cell populations were investigated (Fig. 2f). The CaP USNC treatment enhanced MHC II expression, the costimulatory molecules CD80, and CD115 compared with the HANPs and CON groups (Fig. 2f). In addition, the CaP USNC group showed higher levels of CD25, CD69, CTLA-4, CD80, and Granzyme B in $\gamma\delta$ T cells than the HANP and CON groups (Fig. 2f). Increased pro-inflammatory cytokines expression was detected in the CaP USNC

and HANP groups compared with the CON group (Fig. 2g). CaP USNCs induced higher expression of IL-6, CCL2, and CCL4, while HANPs resulted in higher expression of IL-1 β and IL-2 (Fig. 2g). The CaP USNC group showed higher expression of IL-6, CCL2 and CCL4, while the HANP group showed higher expression of IL-1 β and IL-2 (Fig. 2g). Moreover, the anti-inflammatory cytokine IL-33 was higher in the CaP USNC group (Fig. 2g).

3.3. Adaptive immune activation in blood after 14-day exposure to the two types of CaP NPs

Noticeably, the proportions of monocytes, macrophages,

neutrophils, DCs, and NK cells were all decreased, while the total proportions of adaptive immune cells were higher in the CaP USNC and HANP groups compared with the CON group, indicating that the adaptive immune cells were activated in the blood at day 14 (Fig. 3d and e). For example, the proportion of B cells was increased in both the CaP USNC and HANP groups compared with the CON group (Fig. 3d and e); the proportion of CD8 + T cells was slightly lower in the CaP USNC and HANP groups than in the CON group; and the proportion of CD4 + T cells in the CaP USNC group exceeded those of the HANP and CON groups; there was no obvious difference in the proportion of $\gamma\delta$ T cells among the three groups (Fig. 3e). To explore functional differences in immune subpopulations at day 14, functional markers expression in

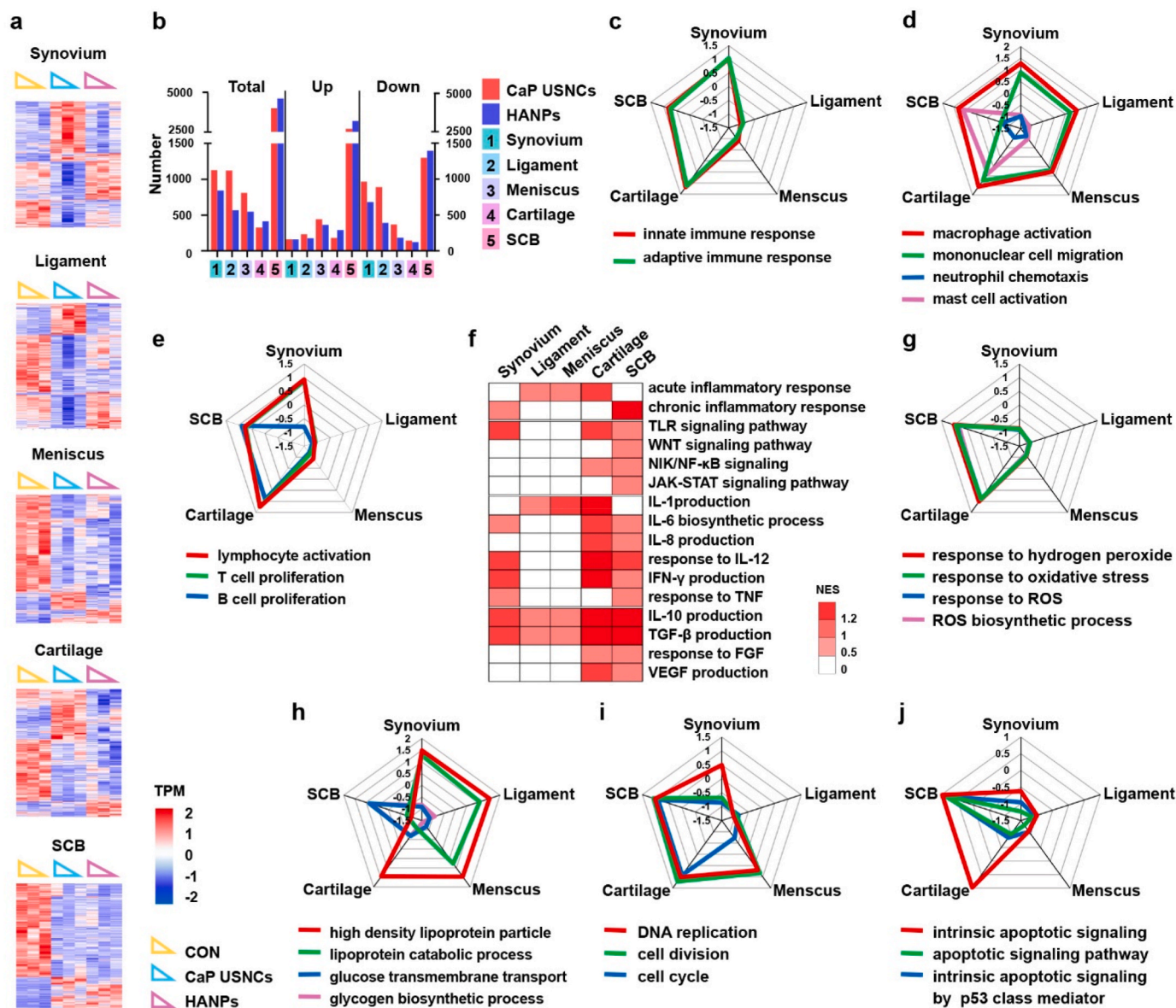


Fig. 4. The biological effects of CaP USNCs on local tissues with whole-tissue gene expression. (a) Heatmaps showed transcript per million (TPM) of the differentially expressed genes (DEGs, $P < 0.05$) from the local tissues among CON, CaP USNCs, and HANPs groups. Red color indicates upregulated genes and blue color indicates downregulated genes. (b) The numbers of DEGs ($P < 0.05$, > 2 -fold changes) of the local tissues upon CaP USNC and HANP treatment compared with CON, respectively. (c) CaP USNCs elicited a strong pro-inflammatory immune response in the synovium, cartilage, and subchondral bone. (d) CaP USNCs drastically increased the level of macrophage activation of myeloid lineages in all five tissues. (e) CaP USNCs induced a strong immune response of the lymphocyte lineages in the cartilage and subchondral bone. (f) CaP USNCs distinctively altered the inflammation signaling pathway, pro-inflammatory and anti-inflammatory cytokines, chemokines, and growth factors. (g) CaP USNCs could induce strong oxidative stress in cartilage and subchondral bone. (h) CaP USNC treatment drastically increased the level of lipoprotein metabolism in the synovium, ligament, meniscus, and cartilage. (i) CaP USNCs activated cell proliferation in the cartilage, subchondral bone, and meniscus. (j) CaP USNC treatment activated the apoptotic signaling pathway and caused cell death in the subchondral bone. (c to j) Compared with the CON group, the NES of each gene ontology term was compared among different tissues upon CaP USNC treatment. SCB: subchondral bone.

various immune cell populations was also investigated (Fig. 3f). The HANP-treated group showed a higher expression of CD28 in CD8 + T cells than the CaP USNC and CON groups (Fig. 3f). The pro-inflammatory cytokines, including CCL2, CCL4, CXCL1, and IL-6, decreased significantly in both the CaP USNC and HANP groups compared with the CON group (Fig. 3g). The anti-inflammatory cytokine IL-4 was significantly increased in the CaP USNC and HANP groups compared with the CON group (Fig. 3g). Furthermore, the anti-inflammatory IL-4 in the CaP USNC group significantly exceeded that of the CON group (Fig. 3g).

3.4. Biological effects of CaP USNCs on local tissues illustrated by whole-tissue gene expression

Using RNA-Seq, we analyzed the body-wide-organ-transcriptomic responses of rats at 3 days post-exposure to the two types of CaP NPs. All the measured samples were clustered by t-distributed stochastic neighbor embedding (t-SNE) (Fig. S11a) and a cluster tree (Fig. S11b), which demonstrated separations between local tissues and major organs. Using xCell from RNA-seq data [27], the two types of CaP NPs mainly affected the immune cell composition in the local tissues and the spleen, with minimum changes in other organs (Fig. S12).

The differentially expressed genes (DEGs) from each tissue were further analyzed, which showed that CaP USNC affected the gene expression levels of all five tissue types compared with CON (Fig. 4a). Among the five tissues, the subchondral bone showed the largest numbers of total influenced genes, upregulated genes and downregulated genes upon CaP USNCs treatment (Fig. 4b).

The CaP USNCs were able to elicit a strong pro-inflammatory immune response in the synovium, cartilage and subchondral bone (Fig. 4c). Regarding the myeloid cells, CaP USNCs treatment increased the levels of macrophage activation in all the five tissues (Fig. 4d). Furthermore, CaP USNCs induced a strong response of lymphocyte-cell-mediated immunity in the synovium, cartilage and subchondral bone (Fig. 4e). Using xCell [27], we found CaP USNCs significantly increased the number of Th2 cells and CD8⁺ T cells in the ligament, but significantly decreased the number of M2 in the meniscus compared with the CON group (Fig. S15). CaP USNCs activated inflammation signaling pathways, such as TLR (Toll-like receptor), Wnt, NF- κ B, and JAK-STAT signaling in the local tissues (Fig. 4f). In addition, CaP USNCs induced the production of proinflammatory cytokines in the synovium (IL-6, IL-12, IFN- γ , and TNF), ligament and meniscus (IL-1), cartilage (IL-1, IL-6, IL-8, IL-12, and IFN- γ) and subchondral bone (IL-6, IL-8, IL-12, and IFN- γ) (Fig. 4f). The levels of anti-inflammatory cytokines in the synovium, ligament, and meniscus (IL-10 and TGF- β) together with cartilage and subchondral bone (IL-10, TGF- β , FGF and VEGF) were increased by CaP USNC treatment (Fig. 4f). Furthermore, compared with the CON group, we observed thickening of the synovial lining layer and increased synovitis scores in the CaP USNC group (Fig. 6b and c), while it restored to a normal level at 14 days (Fig. S6).

CaP USNCs affected other major signaling activities in the local tissues (Fig. S13a). CaP USNCs could also induce a strong response to oxidative stress in the cartilage and subchondral bone (Fig. 4g). CaP USNCs treatment drastically increased the level of lipoprotein metabolism in the synovium, ligament, meniscus and cartilage, as well as the level of glucose metabolism in the subchondral bone (Fig. 4h). The ion channel activities were also altered by CaP USNC treatment in the local tissues (Fig. S13b). Furthermore, our results showed that CaP USNC treatment activated cell proliferation in the cartilage, subchondral bone, meniscus and synovium, while an opposite effect was observed in the ligament (Fig. 4i), which was supported by the number of chondrocytes in the cartilage. By quantitative analysis of chondrocyte numbers (CH) in superficial zone (SZ) or transition and middle zones (TZ + MZ), it was noticed that the number of chondrocytes was increased by CaP USNCs (Fig. 6f and g), but restored to a normal level at 14 days (Fig. S6). Additionally, the epigenetic activities were adjusted by CaP USNC

treatment in the local tissues (Fig. S13c). Last but not least, CaP USNCs activated apoptotic signaling in the cartilage and subchondral bone (Fig. 4j), which was supported by the results of TUNEL immunostaining. By quantitative analysis of the percentages of TUNEL⁺ cells within articular cartilage, it was noticed that the number of apoptotic chondrocytes was increased by CaP USNCs (Fig. 6i and j).

Overall, CaP USNCs demonstrated stronger activation on immune responses, oxidative stress, proliferation and apoptosis in the cartilage and subchondral bone.

3.5. Biological effects of CaP USNCs on major organs illustrated by whole-tissue gene expression

Further analysis based on the RNA-seq data between the CaP USNC-treated and control samples showed that CaP USNCs affected the level of gene expression of all five major organs (Fig. 5a). Among the five organs, spleen exhibited the greatest number of total influenced genes, upregulated genes and downregulated genes upon CaP USNC treatment (Fig. 5b).

CaP USNCs induced a strong response of pro-inflammatory immunity in the heart, liver, spleen and kidney, with the highest normalized enrichment scores (NES) in the spleen (Fig. 5c). For myeloid cells, CaP USNC treatment elevated the level of mast cell activation in all five organs (Fig. 5d). CaP USNC treatment also induced a strong lymphocyte-cell-mediated immune response in the heart, liver, spleen and kidney (Fig. 5e). Additionally, CaP USNCs activated inflammation signaling pathways, such as TLR, NF- κ B, JAK-STAT and WNT signaling, in the major organs. Besides, CaP USNCs induced the production of proinflammatory cytokines in the heart, liver, spleen and kidney (IL-1, IL-6, IL-8, IL-12, IFN- γ and TNF) and lung (IL-1, IL-6 and TNF). Furthermore, the levels of anti-inflammatory cytokines in the heart and spleen (IL-10, TGF- β and VEGF), lung (VEGF), liver (IL-10, TGF- β , FGF and VEGF), and kidney (TGF- β , FGF and VEGF) were increased upon CaP USNC treatment (Fig. 5f).

CaP USNCs impacted on other major signaling activities in the major organs (Fig. S14a). CaP USNCs could induce a strong response to oxidative stress in the liver, spleen and kidney (Fig. 5g). CaP USNC treatment dramatically disturbed the metabolic activities of lipid and glucose in the major organs, with higher NES in the liver (Fig. 5h; Fig. 7g) and kidney (Fig. 5h), supporting by histological assessment and blood biochemical examination. First, we observed higher level of fat accumulation in the liver at 3-day exposure to CaP USNCs comparing to the other groups (Fig. 7h and i), but restored to a normal level at 14 days (Fig. S6). Second, the level of glucose in the blood from the CaP USNCs treated group was significantly increased at 3 days (Fig. 7j), but restored to a normal level at 14 days (Fig. S3b). CaP USNCs also affected the ion channel activities in the major organs (Fig. S14b). Our results illustrated that CaP USNCs could activate cell proliferation in the liver and kidney, while an opposite effect was observed in the heart, lung and spleen (Fig. 5i). The epigenetic activities were altered by CaP USNC treatment in the local tissues (Fig. S14c). Lastly, CaP USNCs activated the apoptotic signaling pathway in the heart, liver, spleen and kidney (Fig. 5j). By quantitative analysis of percentages of TUNEL⁺ cells within the heart, however, it was noticed that CaP USNCs had no obvious effect on the number of apoptotic cells (Fig. S17c).

Overall, CaP USNCs exhibited stronger activated immune responses in the spleen, and stronger oxidative stress, metabolism, proliferation and apoptosis in the liver and kidney.

3.6. Differences in safety between CaP USNCs and HANPs in local tissues

There was a different degree of impact comparing the CaP USNC group to the HANP group on gene expressions in all five tissues (Fig. 4a). Based on the numbers of total influenced genes, upregulated genes and downregulated genes, CaP USNCs had a greater impact on gene expression of the synovium, ligament and meniscus, while less impact

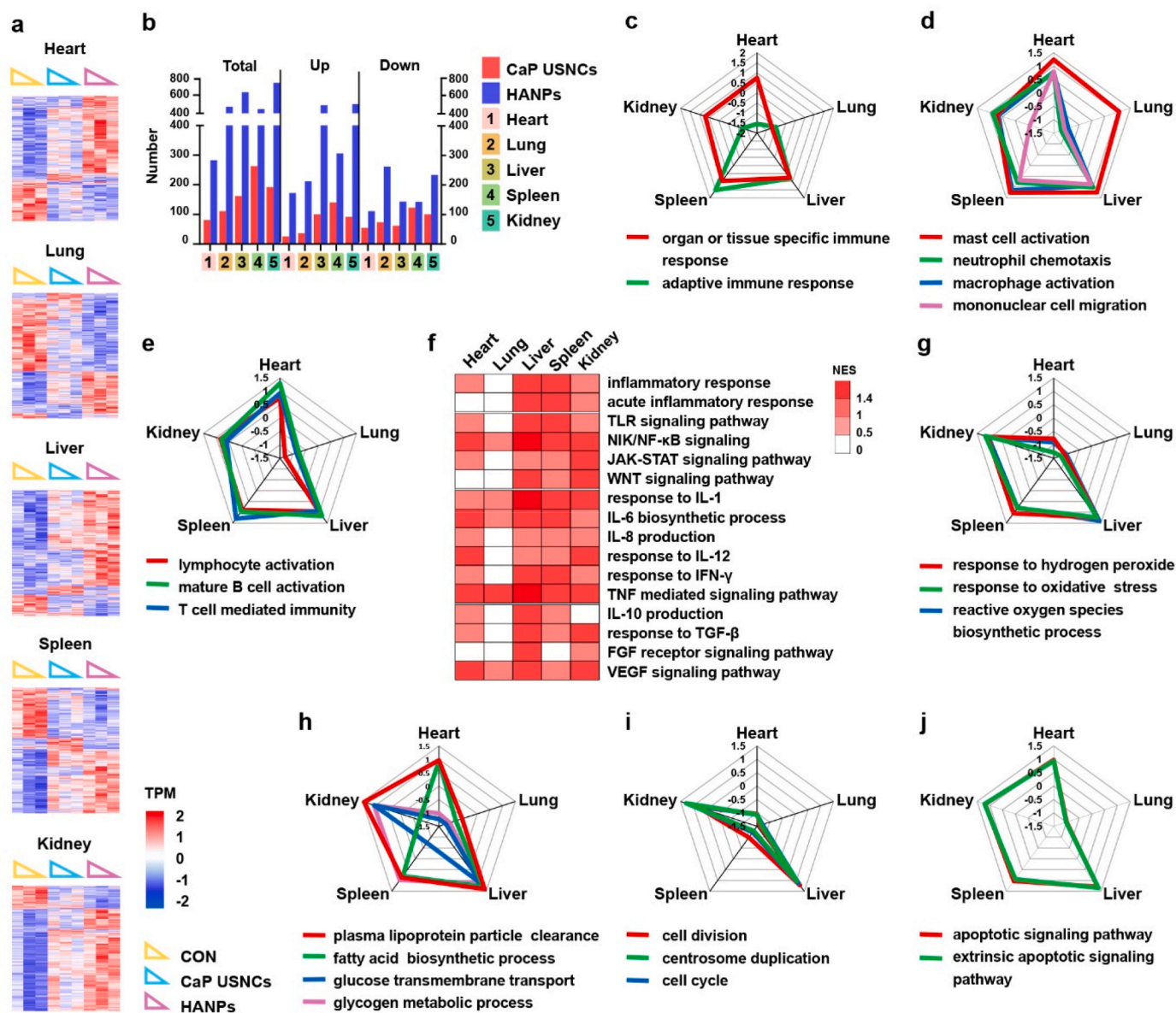


Fig. 5. The biological effects of CaP USNCs on major organs with whole-tissue gene expression. (a) Heatmaps showed transcript per million (TPM) of the differentially expressed genes (DEGs, $P < 0.05$) from the major organs among CON, Ca USNCs, and HANPs groups. Red color indicates upregulated genes and blue color indicates downregulated genes. (b) The numbers of DEGs ($P < 0.05$, > 2 -fold changes) of the major organs upon CaP USNCs, HANPs treatment compared with the CON, respectively. (c) CaP USNCs elicited the strongest pro-inflammatory immune response in the spleen. (d) CaP USNCs drastically increased the level of mast cell activation of myeloid lineages in all the five organs. (e) CaP USNCs induced the strongest T- and B cell mediated immunity in the spleen. (f) CaP USNCs distinctively altered the inflammation signaling pathway, pro-inflammatory and anti-inflammatory cytokines, chemokines, and growth factors. (g) CaP USNCs could induce strong oxidative stress in the liver, spleen, and kidney. (h) CaP USNCs drastically disturbed metabolic activities in the liver and kidney. (i) CaP USNCs activated cell proliferation in the liver and kidney. (j) CaP USNC treatment activated the apoptotic signaling pathway and caused cell death in the heart, liver, spleen, and kidney. (c to j) Compared with CON group, the NES of each gene ontology term was compared among different tissues upon CaP USNC treatment.

on gene expression of the subchondral bone than HANPs (Fig. 4b).

Gene sets related to inflammatory immune responses were downregulated in the synovium and upregulated in the ligament, meniscus, cartilage and subchondral bone for the CaP USNC group. This indicated that CaP USNCs generated inflammatory immune responses in the ligament, meniscus, cartilage and subchondral bone, while HANPs induced an inflammatory immune response in the synovium (Fig. 6a). Using xCell [27], we found that comparing to HANP-treated samples, CaP USNC-treated samples had a larger number of Th2 cells ($P < 0.05$), CD8⁺ T cells ($P < 0.05$) and class-switched memory B-cells ($P > 0.05$) in the ligament, whereas showed lower counts of CLP ($P > 0.05$) in the ligament and DC ($P < 0.05$) cells in the meniscus (Fig. S15). Furthermore, compared with the CON group, we also observed thickening of the

synovial lining layer and increased synovitis scores in the HANP group (Fig. 6b and c), but restored to a normal level at 14 days (Fig. S6).

The different impacts of each signaling pathway between the CaP USNC and HANP groups are shown in Fig. S16a. CaP USNCs induced a strong response of oxidative stress in the cartilage and meniscus, while HANPs induced this effect in the other three tissues (Fig. 6d). CaP USNCs activated cell proliferation in the ligament, meniscus, cartilage and subchondral bone, while HANP treatment activated it in the synovium (Fig. 6e), which was supported by the number of chondrocytes in the cartilage. Compared with the HANP treatment, it was noticed that the number of chondrocytes was significantly increased by CaP USNCs (Fig. 6f and g), but restored to a normal level at 14 days (Fig. S6). The differences in ion channel activities between the CaP USNC and HANP

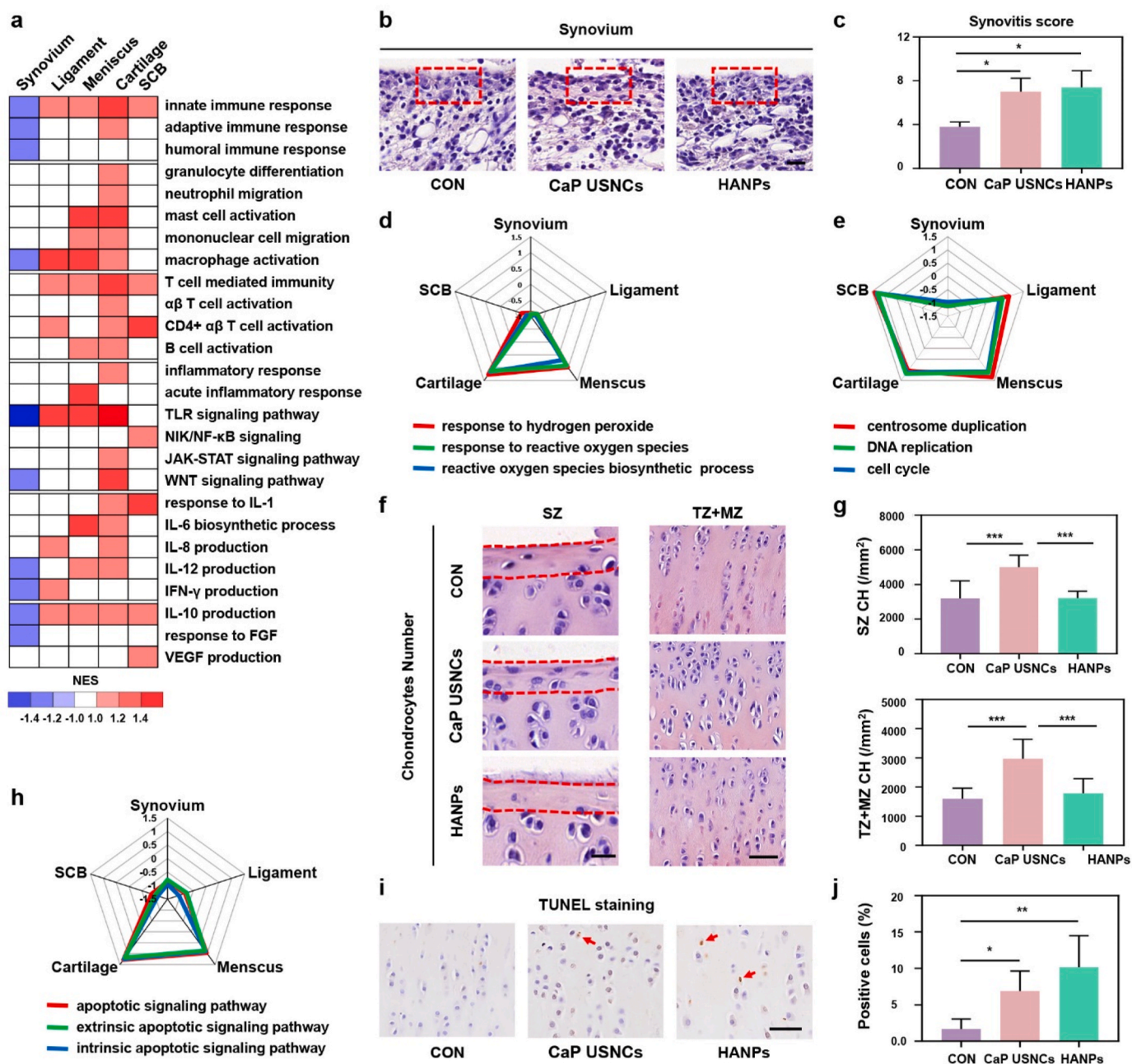


Fig. 6. The differences in biological responses between CaP USNCs and HANPs in local tissues. (a) Different inflammatory immune responses across local tissues between CaP USNCs and HANPs. Red color indicates upregulated gene sets in the CaP USNC group and blue color represents upregulated gene sets in the HANP group. Hematoxylin and eosin (H&E) staining (b) and synovitis score (c) in the synovium from the three groups. Red boxed areas indicate the synovial tissues. $n = 5$. Scale bar, 20 μm . Different impacts on oxidative stress (d) and cell proliferation (e) of each tissue between CaP USNCs and HANPs. (f) H&E staining of superficial zone (SZ) and transition and middle zones (TZ + MZ) from tibial articular cartilage among the three groups. Dashed lines outline SZ for analysis. Scale bar, 20 μm . (g) Chondrocyte numbers (CH) in SZ and TZ + MZ from the three groups. $n = 5$. (h) Different influences on apoptosis of each tissue between CaP USNCs and HANPs. (i) Immunostaining of TUNEL in tibial articular cartilage of rats. Scale bar, 50 μm . (j) The percentages of TUNEL⁺ cells within articular cartilage were quantified. Red arrows indicate TUNEL⁺ cells. $n = 5$. Compared with HANPs, the normalized enrichment scores (NES) in (a), (d), (e) and (h) of each gene ontology term were compared among different tissues upon CaP USNC treatment. SCB: subchondral bone.

groups are shown in Fig. S16b. CaP USNCs triggered metabolic activity in the ligament, cartilage, subchondral bone and meniscus, while HANP treatment triggered it in the synovium (Fig. S16c). CaP USNCs activated epigenetic regulations in the meniscus, cartilage and subchondral bone, while the HANP treatment activated them in the synovium and ligament (Fig. S16d). Lastly, CaP USNCs prompted the apoptotic signaling pathway in the cartilage and meniscus, while the HANPs prompted it in the other three tissues (Fig. 6h). By quantitative analysis of percentages of TUNEL⁺ cells within articular cartilage, it was noticed that the

number of apoptotic chondrocytes was also increased by HANPs (Fig. 6i and j).

3.7. Differences in safety between CaP USNCs and HANPs in major organs

There was a different degree of impact comparing the CaP USNC group to the HANP group on gene expressions in all five organs (Fig. 5a). Based on the numbers of total influenced genes, upregulated genes and

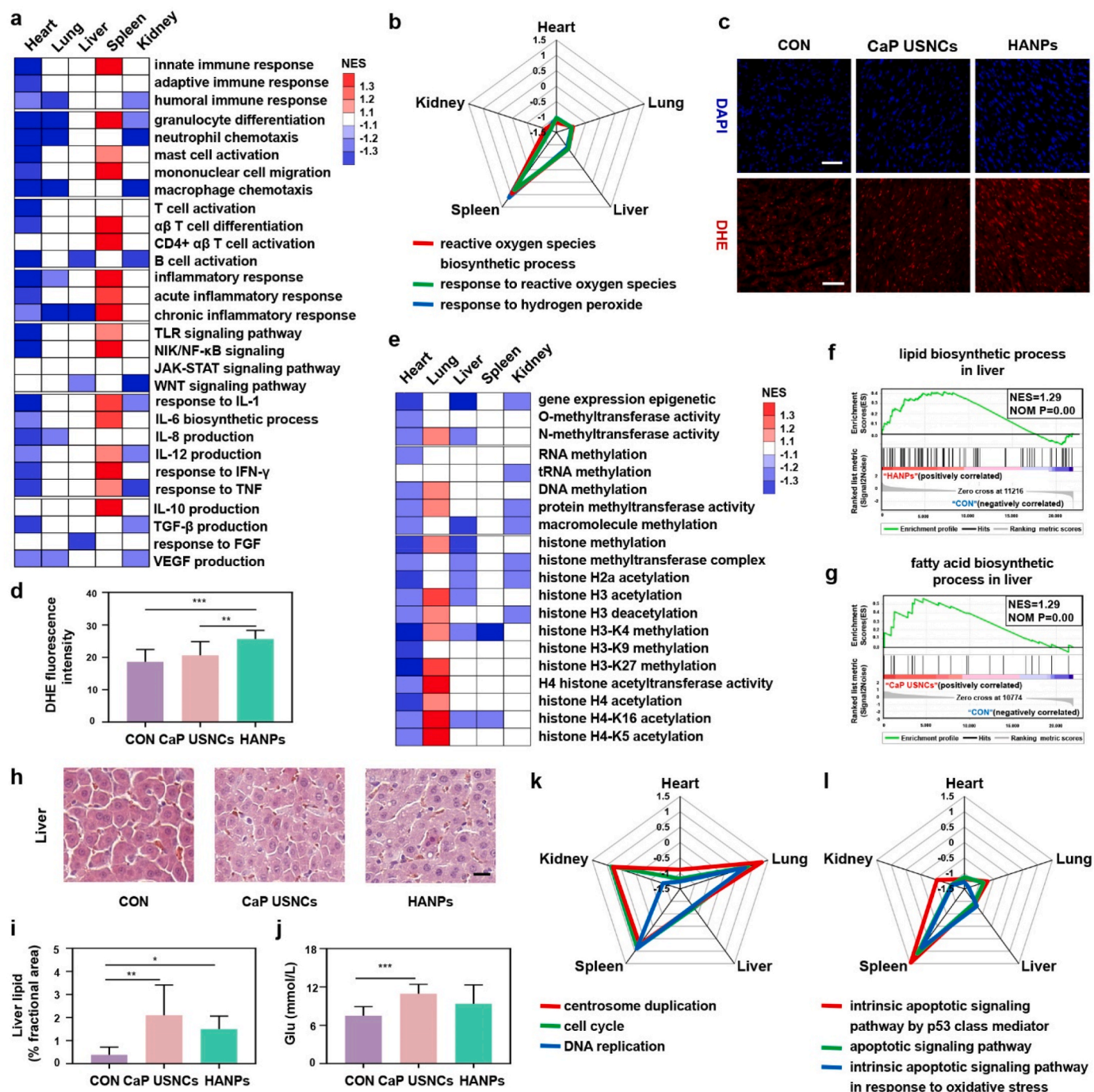


Fig. 7. The differences in safety between CaP USNCs and HANPs in major organs. (a) Different inflammatory immune responses across major organs between the CaP USNC and HANP groups. Red color indicates upregulated gene set in the CaP USNCs group and blue color indicates upregulated gene set in the HANPs group. (b) The differential impacts on oxidative stress across major organs between the CaP USNC and HANP groups. Dihydroethidium (DHE) staining (c) and quantification of DHE signal intensity (d) in the heart from the three groups. $n = 5$. Scale bar = 50 μm . (e) The different levels of epigenetic activities across organs between the CaP USNC and HANP groups. Red color indicates upregulated gene set in the CaP USNCs group and blue color indicates upregulated gene set in the HANPs group. Compared with CON, gene set enrichment analysis (GSEA) associated with metabolic activities from the HANP group (f) and CaP USNC group (g) in the liver. H&E staining images (h) and proportional area with hepatocellular fat (i) in the liver from the three groups. $n = 5$. Scale bar = 20 μm . (j) Levels of glucose in peripheral venous blood of the three groups. $n = 5$. The different activities of cell proliferation (k) and apoptosis (l) across different organs between the CaP USNC and HANP groups. Compared with HANPs, the normalized enrichment scores (NES) in (a), (b), (e), (k) and (l) of each gene ontology term was examined among different tissues upon CaP USNCs.

downregulated genes, CaP USNCs had a less impact on gene expression in all five organs than HANPs (Fig. 5b).

The CaP USNCs treatment induced a strong inflammatory response in the spleen, while HANPs induced an inflammatory immune response in the other four organs (Fig. 7a). The different impacts of each signaling

pathway between CaP USNCs and HANPs are shown in Fig. S17a. CaP USNCs could induce a strong response of oxidative stress in the spleen, while HANPs had such effects in the heart, lung, liver and kidney (Fig. 7b), which was supported by assessing the levels of reactive oxygen species (ROS) production in the heart. By quantitative analysis of

dihydroethidium (DHE) staining of the heart, it was noticed that ROS levels increased by HANPs were higher than those by CaP USNCs (Fig. 7c and d). CaP USNCs elevated epigenetic regulations in the lung, while the HANPs elevated such regulations in the other four organs (Fig. 7e). The differences in ion channel activities between the CaP USNC and HANP groups are shown Fig. S17b. Both CaP NPs had an effect on metabolic activity alterations in major organs (Fig. S17d). HANPs could also trigger the fatty acid biosynthetic process in the liver (Fig. 7f), and subsequently cause more hepatocellular fat accumulation than the CON group (Fig. 7h and i). Furthermore, the glucose level in the blood from the HANPs group increased at 3 days (Fig. 7j) and subsequently restored to a normal level at 14 days (Fig. S3b) compared to the CON group. Our results also demonstrated that CaP USNCs promoted cell proliferation in the lung, spleen and kidney, while HANPs promoted cell proliferation in the heart and liver (Fig. 7k). Lastly, CaP USNCs activated the apoptotic signaling pathway in the spleen, while HANPs had such effect in the other four organs (Fig. 7l). By quantitative analysis of percentages of TUNEL⁺ cells within the heart, however, it was noticed that HANPs had no obvious effect on the number of apoptotic cells (Fig. S17c).

4. Discussion

In this study, the distribution *in vivo* of two types of CaP NPs were evaluated by *ex vivo* imaging of multiple tissues, and the results showed that CaP USNCs were retained not only in the local tissues with maximal accumulation in the meniscus and cartilage, but were also found in other organs with maximal accumulation in the lung and liver at 3-day exposure. Applying CyTOF and the magnetic luminex assay, we identified dynamic systemic responses to CaP USNCs, which began with innate immune activation and followed by adaptive immune activation in the blood circulation via single-cell resolution assays. Subsequently, we studied the acute response of body-wide organ-transcriptomics upon CaP USNCs treatment. We found that CaP USNCs induced stronger activation of immune responses in the local tissues (cartilage and subchondral bone in particular) and spleen, and introduced higher metabolic activities in the liver and kidney of major organs. Lastly, we compared the differences in biosafety between CaP USNCs and HANPs on the body. Based on the immunological response profiles, histological evaluation of major organs and local tissues, and the body-wide transcriptomics overview, we uncovered that CaP USNCs was not more hazardous than HANPs.

To reveal the influence and potential risks of USNCs on biological systems is essential for clinical applications of these novel materials. Multi-omics approaches, which could thoroughly disclose such potential risks and characterize complex cellular responses [16,28], have not been applied to nanomaterials to date. Here, we present a new strategy via single-cell multi-omics analysis to investigate the body-wide systemic responses to USNCs. The CyTOF method with over 40 analysts could assist in dissecting various immune cell populations and functional molecules at single-cell resolution. Additionally, the high-throughput magnetic luminex assay could simultaneously measure up to 20 serum cytokines. Hence, the combination of CyTOF and magnetic luminex assay could facilitate the evaluation of the complex relationship between NPs and the systemic immune responses they initiated. Furthermore, the analysis of the Nano Genome Atlas of multi-tissues enable us to compare the biological functions among different organs and tissues. Therefore, single-cell multi-omics analysis could promote the analysis of body-wide systemic responses of nanomaterials.

The immune system is adept in non-self recognition and thus always interact with NPs [29]. Initially, immune cellular responses were induced by NPs after infiltration into organs and tissues, such as neutrophils and the mononuclear phagocytic system at the early stage [30–32]. In this study, we detected that CaP USNCs significantly increased the proportion of neutrophils, monocyte, macrophage and DCs in the blood and mainly affected immune cell composition in the local tissues and spleen, while caused minimal changes in other organs. In

addition, CaP USNCs mainly induced mast cell activation in the major organs and macrophage activation in the local tissues. DCs, similar to macrophages, phagocytize particles and process danger signals at the injury site [33]. Smaller gold nanoclusters were more efficiently taken up by DCs than larger particles [34,35]. Our studies showed that the proportion of DCs was higher in the CaP USNC group than that in the HANP group in the blood, suggesting that DCs were more sensitive to USNCs compared with the larger HANPs. Further, the proportion of NK cells was also higher in the CaP USNC group than in the HANP group in the blood. The function of NK cells includes the extermination of stressed/abnormal cells and the release of cytokines [36]. In addition to characterize their proportions, the functional responses in immune cells could be determined by CyTOF. The CaP USNCs group demonstrated enhanced expression of antigen presentation-related proteins CD80 and MHC II in macrophages compared with the HANP group, indicating that the CaP USNCs could augment the function of macrophage more effectively. Besides, the macrophage also exhibited higher expression of CD115 by CaP USNCs treatment. It was reported that CD115 is a central component of responses towards foreign body, and its inhibition could prevent host responses [37]. The acute phase of inflammation involves the release of pro-inflammatory cytokines and chemokines [29]. In this study, we also discovered that CaP USNCs upregulated pro-inflammatory cytokines not only in the blood, but also in the local tissues and major organs after 3-day post-exposure, while the effect was reduced after 14-day post-injection.

Compared with HANPs, CaP USNCs induced stronger responses in local tissues, but showed less risk on major organs. The *in vivo* bio-distribution of NPs affects both their efficacy and safety, which are deciding factors as to whether clinical utility or not. In the present study, CaP USNCs mainly concentrated in knee joint, which may induce stronger local responses consequently. The local foreign body response could lead to systemic responses. Based on mass cytometry of the blood, CaP USNCs induced higher proportions of innate immune cells and enhanced cellular function. The immune cells migrating to the local sites may result in more efficient clearance of CaP USNCs in a short time. Although CaP USNCs induced a stronger acute immune response than HANPs, the upregulated innate immune cell proportions and pro-inflammatory cytokines were reduced after 14 days. In addition, the acute response in the local tissue, such as increased synovial lining layer and synovitis scores, came to normal level after 14 days. Furthermore, based on transcriptomics, CaP USNCs showed less risk on major organs compared with HANPs. Therefore, CaP USNC was not more hazardous than FDA-approved HANPs after 14 days *in vivo*.

In previous works, compared with MnO NPs (≈15 nm) and the clinically utilized contrast agent, ultra-small-sized iron oxide NPs (≈3 nm) not only exhibited fewer side effects in a mouse model [15], but also showed no obvious risk for non-human primates [9]. Our previous studies demonstrated the promising performance of CaP USNCs in recovering osteoporotic bone [8] and repairing of tooth enamel following local application [38]. As known, biosafety assessment is critically important for clinical translation. Therefore, the systemic evaluation of USNCs potential effects pave way for further clinical application of CaP USNCs. Our data suggest that CaP USNCs demonstrate differential effects on different tissues regarding proliferation, metabolic and apoptotic processes. Thus, appropriate surface modification of CaP USNCs is required for clinical application to avoid undesirable effects on the body. Alternatively, the ability of CaP USNCs on induction of cell apoptosis at specific tissues may become useful for tumor-targeted therapy. In summary, the current findings collectively suggest that CaP USNCs are safe enough following local application, and could have potential clinical utility as the next-generation of CaP NPs. And the established strategy provides a powerful platform for evaluating the safety of nanomaterials at the organism and cell level.

5. Conclusion

Our results determined that USNCs have differential impacts on different tissues with potential clinical utility as the next-generation NPs. The new strategy established in this study allows us to evaluate the risk levels of different tissues and organs at the whole-organism scale following USNCs treatment.

Author contributions

Tao Zhang: performed the experiments and analyzed the data, co-wrote the manuscript. Tingyun Lei: performed the experiments and analyzed the data, co-wrote the manuscript. Ruojin Yan: assistant in analyzing the data. Bo Zhou: assistant in analyzing the data. Chunmei Fan: assistant in analyzing the data. Yanyan Zhao: performed the in vivo experiments. Shasha Yao: performed the characterization of nanomaterials. Haihua Pan: provided valuable advice. Yangwu Chen: assistant in analyzing the data. Bingbing Wu: provided valuable advice. Yuwei Yang: perform the in vivo experiments. Lijuan Hu: assistant in analyzing the data. Shen Gu: co-wrote the manuscript. Xiaoyi Chen: assistant in the in vivo experiments. Fangyuan Bao: performed the characterization of nanomaterials. Yu Li: performed the characterization of nanomaterials. Hanqi Xie: assistant in analyzing the data, co-wrote the manuscript. Ruikang Tang: conceived the idea and designed the experiments, supervised the research. Zi Yin: conceived the idea and designed the experiments, supervised the research. All authors discussed the results.

Declaration of competing interest

The authors declare that they have no known competing financial interests or personal relationships that could have appeared to influence the work reported in this paper.

Acknowledgements

The authors are grateful to the Core Facilities of Zhejiang University School of Medicine and Analysis Center of Agrobiological and Environmental Sciences of Zhejiang University for their technical assistance. This work was supported by the National Key Research and Development Program of China (2018YFC1105100), NSFC grants (T2121004, 81972099, 82072463, 81871764) and Zhejiang Provincial Natural Science Foundation of China (LZ22H060002, LR20H060001), Fundamental Research Funds for the Central Universities.

Appendix A. Supplementary data

Supplementary data to this article can be found online at <https://doi.org/10.1016/j.bioactmat.2022.03.026>.

References

- Q. Wang, S. Wang, X. Hu, F. Li, D. Ling, Controlled synthesis and assembly of ultra-small nanoclusters for biomedical applications, *Biomater. Sci.* 7 (2) (2019) 480–489.
- B.H. Kim, M. Hackett, J. Park, T. Hyeon, Synthesis, characterization, and application of ultrasmall nanoparticles, *Nanotechnology* 26 (36) (2015) 365102.
- M.S. Bootharaju, W. Baek, S. Lee, H. Chang, J. Kim, T. Hyeon, Magic-sized stoichiometric II-VI nanoclusters, *Small* (2020), e2002067.
- D. Li, X. Zhang, X. Mei, Purification and separation of ultra-small metal nanoclusters, *Adv. Colloid Interface Sci.* 276 (2020) 102090.
- J. Zhao, L. Ge, H. Yuan, Y. Liu, Y. Gui, B. Zhang, L. Zhou, S. Fang, Heterogeneous gold catalysts for selective hydrogenation: from nanoparticles to atomically precise nanoclusters, *Nanoscale* 11 (24) (2019) 11429–11436.
- D. Ni, D. Jiang, H.J. Im, H.F. Valdovinos, B. Yu, S. Goel, T.E. Barnhart, P. Huang, W. Cai, Radiolabeled polyoxometalate clusters: kidney dysfunction evaluation and tumor diagnosis by positron emission tomography imaging, *Biomaterials* 171 (2018) 144–152.
- X. Hu, J. Sun, F. Li, R. Li, J. Wu, J. He, N. Wang, J. Liu, S. Wang, F. Zhou, X. Sun, D. Kim, T. Hyeon, D. Ling, Renal-clearable hollow bismuth subcarbonate nanotubes for tumor targeted computed tomography imaging and chemoradiotherapy, *Nano Lett.* 18 (2) (2018) 1196–1204.
- S. Yao, X. Lin, Y. Xu, Y. Chen, P. Qiu, C. Shao, B. Jin, Z. Mu, N. Sommerdijk, R. Tang, Osteoporotic bone recovery by a highly bone-inductive calcium phosphate polymer-induced liquid-precursor, *Adv. Sci.* 6 (19) (2019) 1900683.
- Y. Lu, G. Zhang, M. Wang, Y. Wu, M. Hackett, H. Chang, X. Hu, N. Lee, J. He, H. Wen, S. Choi, Iron oxide nanoclusters for T₁ magnetic resonance imaging of non-human primates, *Nat. Biomed. Eng.* 1 (2017) 637–643.
- J.B. Raftis, M.R. Miller, Nanoparticle translocation and multi-organ toxicity: a particularly small problem, *Nano Today* 26 (2019) 8–12.
- W.G. Kreyling, W. Möller, U. Holzwarth, S. Hirn, A. Wenk, C. Schleh, M. Schäffler, N. Haberl, N. Gibson, J.C. Schittny, Age-dependent rat lung deposition patterns of inhaled 20 nm diameter gold nanoparticles and their quantitative biokinetics in adult rats, *ACS Nano* 12 (8) (2018) 7771–7790.
- Z. Guo, Y. Luo, P. Zhang, A.J. Chetwynd, H. Qunhui Xie, F. Abdolalpur Monikh, W. Tao, C. Xie, Y. Liu, L. Xu, Z. Zhang, E. Valsami-Jones, I. Lynch, B. Zhao, Deciphering the particle specific effects on metabolism in rat liver and plasma from ZnO nanoparticles versus ionic Zn exposure, *Environ. Int.* 136 (2020) 105437.
- L. Newman, D.A. Jasim, E. Prestat, N. Lozano, I. de Lazaro, Y. Nam, B.M. Assas, J. Pennock, S.J. Haigh, C. Bussy, K. Kostarelos, Splenic capture and in vivo intracellular biodegradation of biological-grade graphene oxide sheets, *ACS Nano* 14 (8) (2020) 10168–10186.
- A.F. Rodrigues, L. Newman, D. Jasim, S.P. Mukherjee, J. Wang, I.A. Vacchi, C. Ménard-Moyon, A. Bianco, B. Fadeel, K. Kostarelos, C. Bussy, Size-dependent pulmonary impact of thin graphene oxide sheets in mice: toward safe-by-design, *Adv. Sci.* 7 (12) (2020) 1903200.
- R. Chen, D. Ling, L. Zhao, S. Wang, Y. Liu, R. Bai, S. Baik, Y. Zhao, C. Chen, T. Hyeon, Parallel comparative studies on mouse toxicity of oxide nanoparticle- and gadolinium-based T₁ MRI contrast agents, *ACS Nano* 9 (12) (2015) 12425–12435.
- K. Paunovska, D. Loughrey, C.D. Sago, R. Langer, J.E. Dahlman, Using large datasets to understand nanotechnology, *Adv. Mater.* 31 (43) (2019), e1902798.
- M. Kadoki, A. Patil, C.C. Thaiss, D.J. Brooks, S. Pandey, D. Deep, D. Alvarez, U. H. von Andrian, A.J. Wagers, K. Nakai, T.S. Mikkelsen, M. Soumillon, N. Chevrier, Organism-level analysis of vaccination reveals networks of protection across tissues, *Cell* 171 (2) (2017) 398–413, e21.
- T. Krausgruber, N. Fortelny, V. Fife-Gernedl, M. Senekowitsch, L.C. Schuster, A. Lercher, A. Nemeč, C. Schmidl, A.F. Rendeiro, A. Berghaler, C. Böck, Structural cells are key regulators of organ-specific immune responses, *Nature* 583 (7815) (2020) 296–302.
- B. Wu, Y. Li, N. Nie, J. Xu, C. An, Y. Liu, Y. Wang, Y. Chen, L. Gong, Q. Li, E. Giusto, V. Bunpetch, D. Zhang, H. Ouyang, X. Zou, Nano genome atlas (NGA) of body wide organ responses, *Biomaterials* 205 (2019) 38–49.
- H. Wu, B. Wu, Z. Sheng, X. Chen, Varitsara Bunpetch, M. Zeng, Y. Ma, J. Huang, H. Ouyang, Single-cell mass cytometry reveals in vivo immunological response to surgical biomaterials, *Appl. Mater. Today* 16 (2019) 169–178.
- M. Orecchioni, D. Bedognetti, L. Newman, C. Fuoco, F. Spada, W. Hendrickx, F. M. Marincola, F. Sgarrella, A.F. Rodrigues, C. Ménard-Moyon, G. Cesareni, K. Kostarelos, A. Bianco, L.G. Delogu, Single-cell mass cytometry and transcriptome profiling reveal the impact of graphene on human immune cells, *Nat. Commun.* 8 (1) (2017) 1109.
- M. Orecchioni, V. Bordoni, C. Fuoco, G. Reina, H. Lin, M. Zoccheddu, A. Yilmazer, B. Zavan, G. Cesareni, D. Bedognetti, A. Bianco, L.G. Delogu, Toward high-dimensional single-cell analysis of graphene oxide biological impact: tracking on immune cells by single-cell mass cytometry, *Small* 16 (21) (2020), e2000123.
- B. Gaudillière, G.K. Fragiadakis, R.V. Bruggner, M. Nicolau, R. Finck, M. Tingle, J. Silva, E.A. Ganio, C.G. Yeh, W.J. Maloney, J.I. Huddleston, S.B. Goodman, M. M. Davis, S.C. Bendall, W.J. Fantl, M.S. Angst, G.P. Nolan, Coordinated surgical immune signatures contain correlates of clinical recovery, *Sci. Transl. Med.* 6 (255) (2014) 255ra131.
- D. Bobo, K.J. Robinson, J. Islam, K.J. Thurecht, S.R. Corrie, Nanoparticle-based medicines: a review of FDA-approved materials and clinical trials to date, *Pharm. Res. (N. Y.)* 33 (10) (2016) 2373–2387.
- C. Trapnell, A.R. Goff, D. Kim, Differential gene and transcript expression analysis of RNA-seq experiments with TopHat and Cufflinks, *Nat. Protoc.* 9 (2012) 2513, 2513.
- M.I. Love, W. Huber, S. Anders, Moderated estimation of fold change and dispersion for RNA-seq data with DESeq2, *Genome Biol.* 15 (12) (2014) 550.
- D. Aran, Z. Hu, A.J. Butte, xCell: digitally portraying the tissue cellular heterogeneity landscape, *Genome Biol.* 18 (1) (2017) 220.
- J. Yan, S.L. Risacher, L. Shen, A.J. Saykin, Network approaches to systems biology analysis of complex disease: integrative methods for multi-omics data, *Briefings Bioinf.* 19 (6) (2018) 1370–1381.
- M. Himly, M. Geppert, S. Hofer, N. Hofstätter, J. Horejs-Höck, A. Duschl, When would immunologists consider a nanomaterial to be safe? Recommendations for planning studies on nanosafety, *Small* 16 (21) (2020), e1907483.
- S. Keshavan, P. Calligari, L. Stella, L. Fusco, L.G. Delogu, B. Fadeel, Nano-bio interactions: a neutrophil-centric view, *Cell Death Dis.* 10 (8) (2019) 569.
- N.J. Gay, M.F. Symmons, M. Gangloff, C.E. Bryant, Assembly and localization of Toll-like receptor signalling complexes, *Nat. Rev. Immunol.* 14 (8) (2014) 546–558.
- M.J. Pallardy, I. Turbica, A. Biola-Vidamment, Why the immune system should be concerned by nanomaterials, *Front. Immunol.* 8 (2017) 544.

- [33] E. Mariani, G. Lisignoli, R.M. Borzi, L. Pulsatelli, Biomaterials: foreign bodies or tuners for the immune response, *Int. J. Mol. Sci.* 20 (3) (2019).
- [34] T.D. Fernández, J.R. Pearson, M.P. Leal, M.J. Torres, M. Blanca, C. Mayorga, X. Le Guével, Intracellular accumulation and immunological properties of fluorescent gold nanoclusters in human dendritic cells, *Biomaterials* 43 (2015) 1–12.
- [35] X. le Guevel, F. Palomares, M.J. Torres, M. Blanca, T.D. Fernandez, C. Mayorga, Nanoparticle Size Influences the Proliferative Responses of Lymphocyte Subpopulations, vol. 5, 2015, pp. 85305–85309, 104.
- [36] L. Müller, S.K. Steiner, L. Rodriguez-Lorenzo, A. Petri-Fink, B. Rothen-Rutishauser, P. Latzin, Exposure to silver nanoparticles affects viability and function of natural killer cells, mostly via the release of ions, *Cell Biol. Toxicol.* 34 (3) (2018) 167–176.
- [37] J.C. Doloff, O. Veiseh, A.J. Vegas, H.H. Tam, S. Farah, M. Ma, J. Li, A. Bader, A. Chiu, A. Sadraei, S. Aresta-Dasilva, M. Griffin, S. Jhunjhunwala, M. Webber, S. Siebert, K. Tang, M. Chen, E. Langan, N. Dholokia, R. Thakrar, M. Qi, J. Oberholzer, D.L. Greiner, R. Langer, D.G. Anderson, Colony stimulating factor-1 receptor is a central component of the foreign body response to biomaterial implants in rodents and non-human primates, *Nat. Mater.* 16 (6) (2017) 671–680.
- [38] C. Shao, B. Jin, Z. Mu, H. Lu, Y. Zhao, Z. Wu, L. Yan, Z. Zhang, Y. Zhou, H. Pan, Z. Liu, R. Tang, Repair of tooth enamel by a biomimetic mineralization frontier ensuring epitaxial growth, *Sci. Adv.* 5 (8) (2019), eaaw9569.